OPEN ACCESS
IOP Publishing
Journal of Physics B: Atomic, Molecular and Optical Physics
J. Phys. B: At. Mol. Opt. Phys. **58** (2025) 105502 (13pp)
https://doi.org/10.1088/1361-6455/add77a

Strongly confined atomic excitation localization in a weakly-driven atom-waveguide interface

Shao-Hung Chung[1,*], **Wei Chen**[1,2] and **H H Jen**[1,3,4]

[1] Institute of Atomic and Molecular Sciences, Academia Sinica, Taipei 10617, Taiwan
[2] Department of Physics and Center for Quantum Science and Engineering, National Taiwan University, Taipei 10617, Taiwan
[3] Molecular Science and Technology Program, Taiwan International Graduate Program, Academia Sinica, Taipei 10617, Taiwan
[4] Physics Division, National Center for Theoretical Sciences, Taipei 10617, Taiwan

E-mail: ryan2031823@gmail.com

Received 9 February 2025, revised 27 April 2025
Accepted for publication 12 May 2025
Published 27 May 2025

Abstract

An atomic array coupled to a photonic crystal waveguide forms a strongly coupled quantum interface, exhibiting various intriguing collective features of quantum dynamics. Here we consider a homogeneous atomic array and theoretically investigate its steady-state distribution when the incident fields drive the atoms from both sides at asymmetric angles. This effectively creates an interface shared by two zones of atoms under different driving angles. This setup introduces a competition between photon-mediated dipole–dipole interactions and the directionality of coupling, while differences of the traveling phases from the incident angles further influence the overall steady-state behavior. Under this asymmetric driving scheme, the presence of strongly confined localization can be identified, where localization can occur either at the interface or at one of edges. Additionally, we examine the size effect on the atomic localization, deriving an empirical formula to predict parameter regimes that favor interfaced localization. We also consider a defect-driving scheme, where a third zone is created by undriven atoms under symmetric traveling phases. This results in strongly confined single-site excitation localization, which can be explained through analytical solutions under the reciprocal coupling. Finally, we propose several methods for precise control of multiple single-site localizations under the defect-driving scheme. Our results provide insights into driven-dissipative quantum systems with nonreciprocal couplings and pave the way for quantum simulation of exotic many-body states relevant to quantum information applications.

Keywords: atomic localization, photonic crystal waveguide, driven-dissipative quantum system

* Author to whom any correspondence should be addressed.

1. Introduction

Chiral-coupled atomic systems constitute a compelling platform in atom-waveguide quantum electrodynamics [1–8], enabling engineering over the directionality of light propagation. This breaks the time-reversal symmetry in light–matter couplings and establishes effective nonreciprocal decay channels. For instance, unidirectional coupling can be achieved through spin–momentum locking [9], while these decay channels can be tuned by applying external magnetic fields [2, 7, 10–12], thereby allowing control of light transmission based on the quantum emitter's internal state. Such controlled and highly efficient nonreciprocal coupling between atoms has been demonstrated in strongly coupled systems, including artificial quantum emitters [13–18], atom-nanofiber [10, 19–21], atom-photonic crystal waveguide [16, 22], and diamond nanophotonic platforms [23, 24].

Under external laser driving, these platforms form distinctive driven-dissipative open quantum systems [19, 25–32]. The interplay between dissipation and interaction strengths facilitates the emergence of novel quantum many-body states and a wealth of dynamical phenomena. Examples include nontrivial collective radiation [33–42], population localization and delocalization [43–46], and enhanced quantum correlations [47–51] induced by photon-mediated long-range dipole–dipole interactions [20], which generate strongly correlated steady states with potential applications in quantum information processing. This leads to diverse applications, such as photon routing and interference [52], essential for integrated quantum networks and scalable quantum computation [16, 22]. The extra degree of freedom in controlling coupling directionality [10] provides fresh insights into quantum dynamics at these interfaces and paves the way for innovative applications in quantum simulation and quantum computation within next-generation nanophotonic devices.

Recent studies have theoretically employed laser fields incident at Bragg angles to drive the atom-nanofiber system [53], with a focus on pronounced resonance of light scattering through a chiral waveguide. The other work has configured a one-dimensional (1D) atomic array in an anti-Bragg periodic layout under strong coherent driving [54]. This setting reveals strong subradiant eigenstates featuring long-lived quantum correlations between qubits. In addition, a wide range of intriguing delocalization and localization behaviors has been observed through integrating arrays with a clean and a disordered zone [43, 46] or with disparate interparticle spacings [44, 45]. Motivated by the aforementioned studies, here we propose an even straightforward setting in creating a dissimilar driven-dissipative atomic arrays by driving the equidistant atomic array with different incident angles, as shown in figure 1. The previous works of constructing dissimilar atomic arrays focus on designing two different periodic interparticle distances, where an interplay between two distinct photon-mediated dipole–dipole interactions emerges, while in this work our setting with asymmetric driving conditions focuses on the effect from two different incident fields. We anticipate that the phase differences play a vital role in generating interference effects, potentially leading to various intriguing steady states. In certain cases, we observe behaviors reminiscent of those found in a dissimilar array [44], along with precisely controllable and strong population localization. Notably, such localization effects have also been observed in Rydberg atom systems [55], where frequency shift compensation is applied with standing-wave control fields in a cavity to realize a strong Rydberg-state localization with partial or full antiblockade mechanism. In contrast to controlling two fields in the cascade atomic level configurations, our scheme concerns only two-level atomic structures with single laser field. While the [55] adopts the Blockade mechanism mediated by Rydberg levels and tends to finetune the van der Waals interactions with atomic density to achieve strong Rydberg atom localization, our scheme only utilizes asymmetric light incident angles to fulfill the strong atomic localization at the excitation interface. We investigate various parameters and measures to study strongly confined atomic localization under different excitation schemes, supported by analytical solutions under the reciprocal coupling regime. Our results provide deeper insights into interaction-driven atomic excitations within driven-dissipative systems and open new pathways for the realization of exotic quantum states relevant to quantum information processing.

The structure of this paper is organized as follows: section 2 outlines the theoretical framework for a driven-dissipative atomic array with chiral couplings. In section 3, we present the steady-state distribution of atomic excitations under asymmetric incident angles and investigate strong interfaced localization arising from different angle combinations. In section 4, we propose a new scheme with defect driving aimed at enhancing atomic population control and concentration. Finally, section 5 discusses the implications of our findings and concludes the study.

2. Theoretical model

This study investigates a chiral coupling interface formed by a driven 1D atomic array and a photonic crystal waveguide in figure 1(a). The atomic array comprises N identical two-level atoms (or, more generally, two-level quantum emitters, such as superconducting qubits or quantum dots [1]) arranged with a uniform interparticle spacing d. The photonic crystal waveguide acts as a 1D reservoir [12, 47], transmitting photons in guided modes to mediate the coupling between the atoms through evanescent waves [9]. Laser fields drive the atoms individually from the side, propagating in a horizontal plane at the same height as the array, which is parallel and close to the $\hat{x}$–$\hat{y}$ plane.

The dynamical evolution of the system's state ρ is governed by the effective chiral Lindblad master equation [12, 56] in the interaction picture and under the Born–Markov approximation [57],

$$\frac{\mathrm{d}\rho}{\mathrm{d}t} = -\frac{\mathrm{i}}{\hbar}\left[H_{\mathrm{S}} + H_{\mathrm{L}} + H_{\mathrm{R}}, \rho\right] + \mathcal{L}_{\mathrm{L}}\left[\rho\right] + \mathcal{L}_{\mathrm{R}}\left[\rho\right] + \mathcal{L}_{\mathrm{ng}}\left[\rho\right], \tag{1}$$

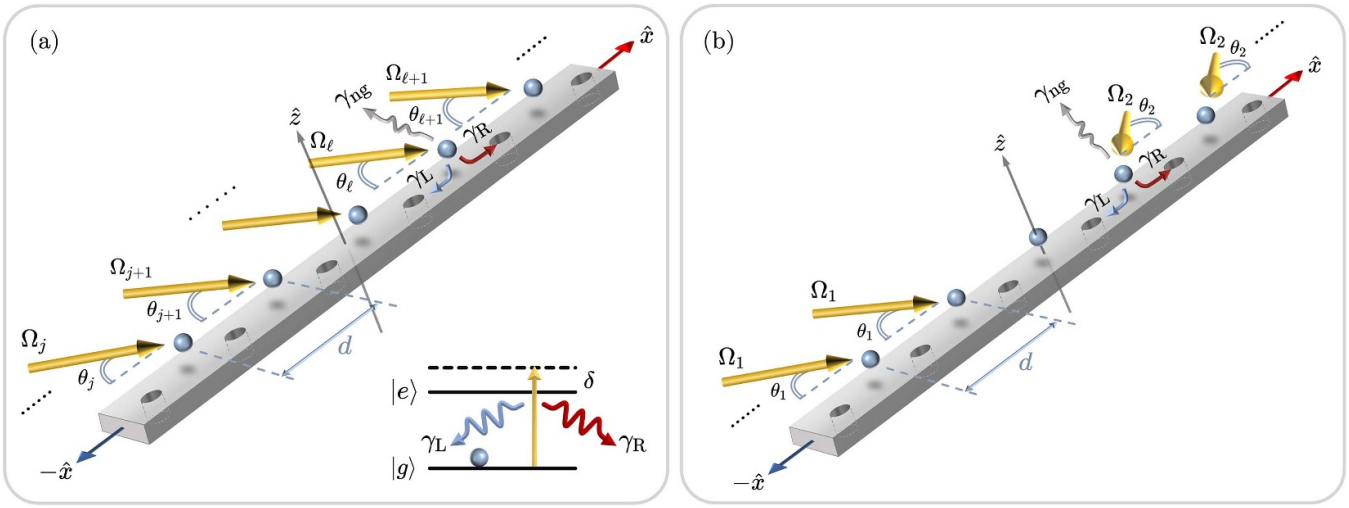

Figure 1. A schematic diagram of a weakly-driven chiral-coupled atomic array. The system consists of a homogeneous one-dimensional array of N two-level quantum emitters with interparticle distance d, coupled to a photonic crystal waveguide. The effective nonreciprocal decay rates $\gamma_L \neq \gamma_R$ are realized through the guided modes in the waveguide and can be controlled by external magnetic fields, while the non-guided decay γ_{ng} determines the coupling efficiency. (a) Generalized model: Each atom is weakly driven and excited laterally by laser fields with varying Rabi frequencies $\{\Omega_j | j = 1, 2, \cdots, N\}$, where δ represents the detuning from the side excitation. (b) Defect-driving scheme: The driving on one of the atoms is removed, and the left and right chains, centered around this atom, are driven at incident angles θ_1 and $\pi - \theta_2$, respectively.

with Hamiltonians H_S the light–matter interaction from a laser field, $H_{L(R)}$ the chiral couplings, and Lindblad forms of $\mathcal{L}[\rho]$ indicating the dissipations. The term H_S is

$$H_S = \hbar \sum_{j=1}^{N} \left[\left(\Omega_j e^{ikx_j \cos\theta_j} \sigma_j + \text{h.c.} \right) - \delta_j \sigma_j^\dagger \sigma_j \right], \tag{2}$$

which drives N two-level quantum emitters (each characterized by the ground state $|g\rangle_j$ and excited state $|e\rangle_j$), with $\Omega_j = \tilde{\Omega}_j e^{i\phi_j}$, where $\tilde{\Omega}_j = |\Omega_j|$ and ϕ_j is the corresponding phase for the jth atom. The phase factor of $\cos\theta_j$ emerges due to the traveling phase differences of the wave front experienced by the atoms under the plane-wave excitations. The emitters are subject to spatially dependent detunings δ_j. The dipole operator is defined as $\sigma_j^\dagger \equiv |e\rangle_j\langle g|$ with $\sigma_j = (\sigma_j^\dagger)^\dagger$. The wave number denotes as $k = 2\pi/\lambda$ with the wavelength λ, while the incident angle at jth atom denoted as θ_j characterizes the propagation phases of the laser field. Notably, under normal incidence, where $\cos\theta_j = 0$, H_S contains no position-dependent phase terms. With identical ϕ_j, the corresponding phases can be factored out as a global phase, leaving the observable outcomes unaffected. In contrast, under oblique incidence, the position-dependent phase $kx_j \cos\theta_j$ plays a significant role in both the system's evolution and its steady-state behaviors. Although different choices of the coordinate origin seem to induce distinct system behaviors, these effects can, in principle, be neutralized by appropriately adjusting $\{\phi_j\}$. This flexibility in phase tuning enhances the versatility of the platform, enriching the possibilities for system control and application.

The coherent terms H_L and H_R are

$$H_{L(R)} = -i\hbar \frac{\gamma_{L(R)}}{2} \sum_{j<(>)\ell}^{N} \left(e^{ik|x_j - x_\ell|} \sigma_j^\dagger \sigma_\ell - \text{h.c.} \right), \tag{3}$$

which represents the collective energy shifts due to the infinite-range photon-mediated dipole–dipole interactions [20, 58], and we label the positions of spins such that $x_j > x_\ell$ when $j > \ell$. The remaining Lindblad terms read

$$\mathcal{L}_\alpha[\rho] = \sum_{j,\ell}^{N} \gamma_{j\ell}^{\alpha} \left[\sigma_\ell \rho \sigma_j^\dagger - \frac{1}{2} \left\{ \sigma_j^\dagger \sigma_\ell, \rho \right\} \right], \tag{4}$$

where $\mathcal{L}_{L(R)}[\rho]$ represents the collective decay in guided modes with decay rates $\gamma_{j\ell}^{L(R)} \equiv \gamma_{L(R)} e^{+(-)ik(x_j - x_\ell)}$, using the subscripts L (R) to label the decay channels that propagate to the left (right). While $\mathcal{L}_{ng}[\rho]$ corresponds to the non-guided decay experienced by the atoms, with decay rate $\gamma_{j\ell}^{ng} \equiv \gamma_{ng}\delta_{j\ell}$, which is intrinsic and is considered to be the same for all identical atoms. For instance, in an atom-nanofiber system, approximately 99% of light is typically scattered due to free-space decay [1]. In contrast, in systems where quantum dots or superconducting qubits are coupled to a photonic crystal waveguide, free-space scattering can be reduced to around 0.5% on average [1, 14, 16], yielding significantly enhanced coupling efficiency. To quantify the tendency of chiral coupling arising from the competition between γ_R and γ_L, the directionality of the couplings $D \equiv (\gamma_R - \gamma_L)/\gamma$ [10] is introduced. Here, the total guided decay rate can be written as $\gamma \equiv \gamma_R + \gamma_L \equiv$

$2|\mathrm{d}q(\omega)/\mathrm{d}\omega|_{\omega=\omega_{\mathrm{eg}}} g_k^2 L$ [47], where $|\mathrm{d}q(\omega)/\mathrm{d}\omega|_{\omega=\omega_{\mathrm{eg}}}$ represents the inverse of group velocity at resonance, with the atom-waveguide coupling strength g_k and the quantization length L.

We note that the usage of 'nonreciprocal' coupling refers to the possibility of unequal left- and right-propagating decay channels, while 'chiral' coupling sometimes refers to the special case of 'unidirectional' decay channel, where only the left- or right-propagating decay channel survives. Meanwhile, 'chiral' coupling also indicates the designated decay channels to the left and to the right, indicating two opposite subjects that cannot be superposed as for our two hands or two orthogonal light polarizations in free space, which is the helicity for massless particles in the case of light. Therefore, throughout the paper, we use them alternatively to represent the couplings other than the reciprocal ones.

We initialize the system in the ground state $|g\rangle^{\otimes N}$, and consider the system dynamics under weak excitation, namely $\Omega_j \ll \gamma_{j\ell}^{\alpha}$ [53]. This assumption confines dynamical evolution to a self-consistent Hilbert subspace $\{|g\rangle^{\otimes N}, |\psi_j\rangle = |e\rangle_j |g\rangle^{\otimes(N-1)}\}$ for $j \in [1,N]$, restricted to the ground state and the manifold of singly excited states. Thus, the total state can be written as

$$|\Psi(t)\rangle = \frac{1}{\sqrt{1+\sum_{j=1}^{N}|p_j(t)|^2}}\left[|g\rangle^{\otimes N} + \sum_{j=1}^{N} p_j(t)\,|\psi_j\rangle\right], \tag{5}$$

where $p_j(t)$ represents the probability amplitude and $\sum_{j=1}^{N}|p_j(t)|^2 \ll 1$ to satisfy the weak-excitation assumption. Thus equation (1) can be reduced to the coupled equations for $p_j(t)$ [59] as

$$\dot{p}_j = -\mathrm{i}\Omega_j \mathrm{e}^{\mathrm{i}k\phi_j}\mathrm{e}^{\mathrm{i}kx_j\cos\theta_j} + \sum_{j=1}^{N}[\mathbf{M}]_{j\ell}\,p_j, \tag{6}$$

where the matrix elements of the coupling matrix $\mathbf{M}$ are:

$$[\mathbf{M}]_{j\ell} = \begin{cases} -\gamma_{\mathrm{L}}\mathrm{e}^{\mathrm{i}k|x_j - x_\ell|} & , j < \ell \\ \mathrm{i}\delta_j - \frac{\gamma_{\mathrm{L}}+\gamma_{\mathrm{R}}+\gamma_{\mathrm{ng}}}{2} & , j = \ell \\ -\gamma_{\mathrm{R}}\mathrm{e}^{\mathrm{i}k|x_j - x_\ell|} & , j > \ell. \end{cases} \tag{7}$$

We then define the dimensionless interparticle distance $\xi \equiv k(x_j - x_{j-1})$. Consequently, the steady-state probability amplitudes, satisfying $\dot{p}_j = 0$, are given by

$$\tilde{p}_j \equiv p_j(t\to\infty) = \mathrm{i}\sum_{\ell=1}^{N}\left[\mathbf{M}^{-1}\right]_{j\ell}\Omega_\ell \mathrm{e}^{\mathrm{i}\phi_\ell}\mathrm{e}^{\mathrm{i}kx_\ell\cos\theta}. \tag{8}$$

We note that under a weak excitation limit, the singly excited states are sufficient to describe the system dynamics. Alternatively speaking, an effective non-Hermitian Hamiltonians can be used to derive equation (6) with a state basis of equation (5), which is equivalent to using equation (1) without the jump operators.

From equations (6), (7), and (8), we can identify interaction-driven quantum behaviors of atomic excitations, primarily governed by the directionality D, photon-mediated dipole–dipole interactions quantified by ξ, and the incident angular configurations $\{\theta_j\}$. In the following sections, we proceed to characterize the localized steady states that emerge within a homogeneous atomic array under different driving schemes, and we further investigate the strongly confined atomic localization achievable within specific parameter regimes under strong coupling efficiency. We note that for high enough coupling efficiency more than 99%, that is for superconducting transmon qubit (with $\gamma_{\mathrm{ng}}/\gamma = 0.001$) or quantum dot-PCW (photonic crystal waveguide with $\gamma_{\mathrm{ng}}/\gamma = 0.01$) [1], our presented results are valid and the predicted strongly confined atomic excitation are kept intact. Meanwhile, for platforms with low coupling efficiency such as Cs atoms coupled to an alligator waveguide (with $\gamma_{\mathrm{ng}}/\gamma = 0.5$) or Rb atoms coupled with a nanofiber (with $\gamma_{\mathrm{ng}}/\gamma = 0.9$), the atomic excitation can still manifest localization features, but not as significant as we anticipate in the strong coupling regimes. Lastly, our model for system dynamics is generic for the above-mentioned platforms, where $\gamma = 2\pi \times 10 - 100$ MHz, 0.2 GHz, and 6 MHz [1] for superconducting transmon qubits, quantum dots, and Rb atoms, respectively.

3. Asymmetric driving scheme

3.1. Steady-state distribution

In this section, we obtained the steady-state distribution for a 1D homogeneous array consisting of N atoms under the asymmetric driving scheme at resonance, i.e. $\delta_j = 0$. We denote the incident angles as

$$\theta_j = \begin{cases} \theta_1 & , j \in [1,m] \\ \theta_2 & , j \in [m+1,N] \end{cases}, \tag{9}$$

where $m = \lceil N/2 \rceil$. Additionally, we consider the Rabi frequencies of the laser fields from both sides to be $\tilde{\Omega}_1 = \tilde{\Omega}_2$ and set $\phi_{1(2)} = -k_0 x_1 \cos\theta_{1(2)}$. This setup uses the first atom's position as the coordinate reference point. Under these conditions, we performed numerical calculations for the normalized steady-state population distribution $\tilde{P}_j$ defined as

$$\tilde{P}_j \equiv \frac{|\tilde{p}_j|^2}{\sum_{j=1}^{N}|\tilde{p}_j|^2}. \tag{10}$$

Concerning the simplest case of a homogeneous array subjected to uniform normal incidence $\theta_1 = \theta_2 = \pi/2$, we obtained the steady-state phase diagram in the parameter space (D,ξ) [59] using the inverse participation ratio (IPR) [60], defined as

$$\mathrm{IPR} \equiv \frac{\sum_{j=1}^{N}\left(\Delta\tilde{P}_j\right)^2}{\left(\sum_{j=1}^{N}\Delta\tilde{P}_j\right)^2}, \tag{11}$$

where $\Delta\tilde{P}_j = |\tilde{P}_j - N^{-1}|\Theta(\tilde{P}_j - N^{-1})$ with the Heaviside step function Θ. It indicates that one of the $\Delta\tilde{P}_j$ dominates as

IPR $\to 1$, signifying strong localization. Conversely, delocalized behaviors are recognized as IPR $\to N^{-1}$. We classified five distinguishable steady-state phases through the phase diagram [59], which are

(1) uniformly extended distributions (ETD) when $\xi \approx 0$;
(2) the crystalline ordered (CO) phase possessing an finite structure factor, mostly for a finite D;
(3) the bi-edge (BE) excitations;
(4) the bi-hole excitations (BH) with hole excitations at the edges mostly for low D; and
(5) the chiral-flow dichotomy when $\xi = \pi$, which depends on the parity of N: a linear slope for an even N and a concave curve for an odd N.

Among these, the ETD, CO, and BH phases exhibit delocalized characteristics, while the BE phase demonstrates localized properties. Furthermore, two critical parameters of reciprocal coupling ($D = 0$) with $\xi = \{0\,(2\pi), \pi\}$ can be identified and excluded from the steady-state phases. This exclusion is due to constructive interference in state populations—a characteristic of decoherence-free space [61] being predominantly populated. This leads to a breakdown of the weak-excitation assumption. In the case of dissimilar arrays formed by two segments with different interparticle spacings [44, 45], the steady-state population distribution is mostly determined by a combination of the five aforementioned steady states, as expected. However, a few combinations exhibit new localized patterns such as half-depletion (HD) phases due to the presence of the interface atom. This highlights the complexity and the effect of interfaces within interacting quantum systems.

In figure 2, we demonstrate the steady-state population distribution $\{\tilde{P}_j\}$ for $N = 50$ in terms of parameter space $(\xi, D, \theta_1, \theta_2)$, where some of the cross-section plots are illustrated in figure 3. In figures 2(e) and (f), we observe a clear boundary in the steady-state population between the mth and $(m+1)$th atoms, leading to a steady-state distribution resembling that in a dissimilar array [44]. This phenomenon is more clearly illustrated in cross-sections of figure 2(e), as displayed in figure 3(c). Under asymmetric driving, unexpected steady-state distributions emerge, such as CO–CO configurations and even a HD-like combination of a soliton-like and a depleted state. These distributions showcase that most of the atomic populations tend to distribute in one of the segments under unidirectional coupling. By contrast, figures 2(a), (b) and (d) showcase a widespread range of interfaced localization, particularly in the lower values of D and ξ. Specifically, the green bar shown in figure 3(a), corresponding to Figure 2(a) at $\xi = 0.05\pi$, indicates that the population is strongly confined at the mth and $(m+1)$th atoms. Essentially, the two-site localization can be further manipulated to shift to different locations by simply adjusting the interface position via external laser drivings, allowing for precise control over the localization. As a comparison, the system reaches a steady state of BE excitation (with $\tilde{P}_{1,N} \approx 0.314$ and $\tilde{P}_{j\neq 1,N} \approx 0.0078$) when driven by a uniform normal incidence under the same parameters $\{D, \xi\}$ of green bars in figure 3(a). Interestingly, the localized

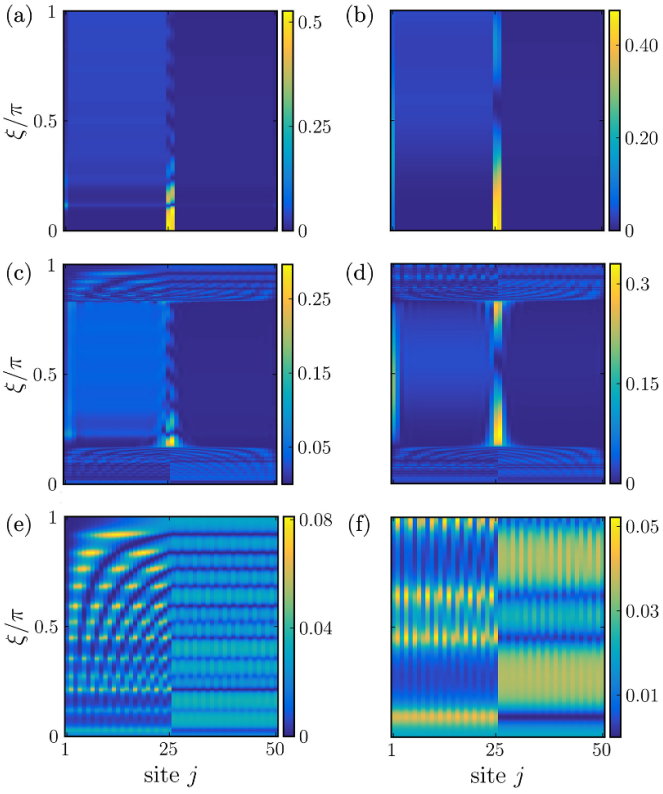

Figure 2. The steady-state population distributions $\tilde{P}_j$ for $N = 50$ atoms, subject to the asymmetric driving scheme. The distributions are presented as a function of ξ, with varying angular configurations (θ_1, θ_2) and directionality D. Panels (a), (c), and (e) correspond to $(\theta_1 = \pi/2, \theta_2 = \pi/4)$, while (b), (d), and (f) represent $(\theta_1 = \pi/4, \theta_2 = \pi/6)$. The directionality D is set to 0, 0.5, and 1 for [(a), (b)], [(c), (d)], and [(e), (f)], respectively, as comparisons.

population can be shifted from the edges and concentrated on the two interface atoms simply by applying external fields at asymmetric angles.

We note that for the dependence of the steady-state population distribution on the atom number, we observe that overall the steady-state population distribution exhibits similar patterns as N increases. However, upon closer inspection, the distribution becomes increasingly sensitive to small variations of interparticle distances, due to the enhanced influence of photon-mediated dipole–dipole interactions in larger systems with more atoms involved, as well as the influence from traveling phases depending on the driving angles. This sensitivity is particularly pronounced under unidirectional coupling conditions ($D = 1$), where more features show up as interparticle distance varies, showing an intricate interplay between N and ξ. This feature of atom number dependence also emerges in figure 4 on the properties of IPR and IIPR, which we will discuss in the next subsection.

3.2. *Strongly confined localization*

Next, we seek to delineate the parameter regions where localization emerges. This can be achieved using the IPR defined

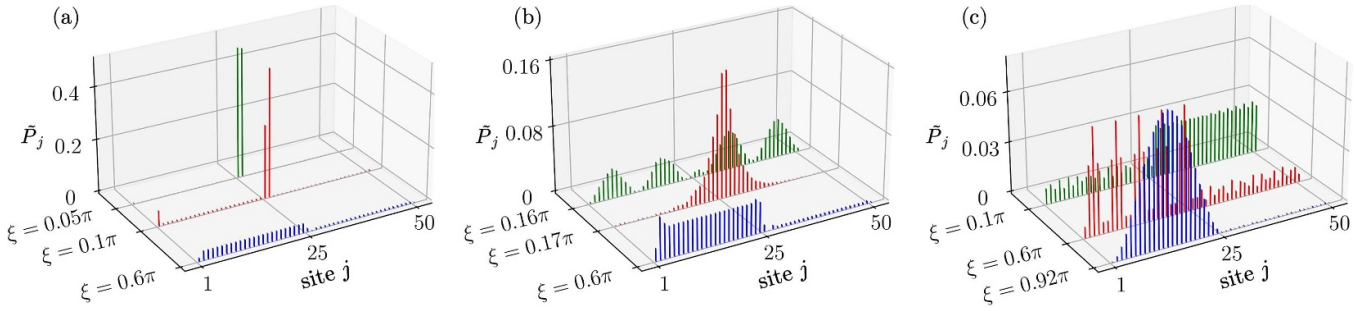

Figure 3. Some examples of steady-state population distributions $\tilde{P}_j$. Panels (a), (b), and (c) correspond to specific cross-sections from figures 2(a), (c), and (e), respectively. In panel (a), for some certain values of ξ (e.g. 0.05π and 0.1π), strongly confined localization at the interface atoms can be observed. Other confined localizations, though not as extreme as in (a), can also be observed in panels (b) and (c). These soliton-like distributions appear at the center or in the other half of the array.

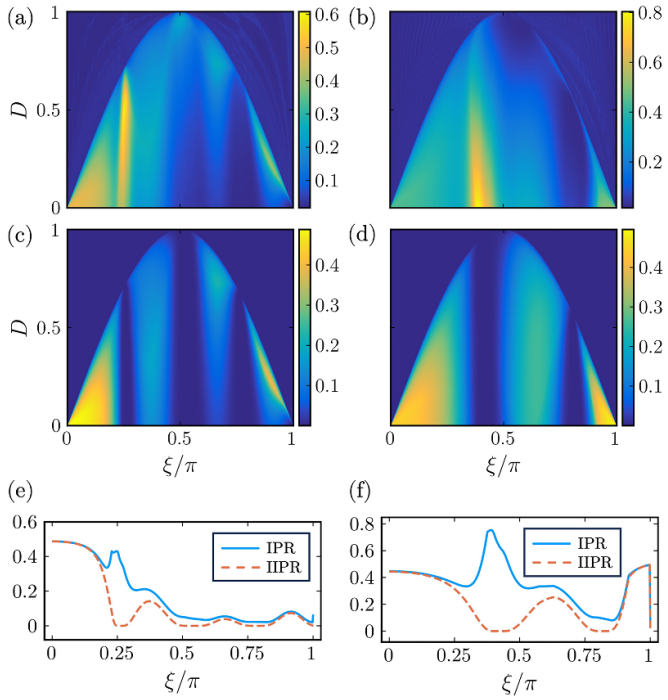

Figure 4. In the asymmetry-driven scheme, the inverse participation ratio (IPR) and interface inverse participation ratio (IIPR) distributions are presented for $N = 100$ atoms. Panels (a) and (c) show the IPR and IIPR respectively at $(\theta_1 = \pi/4, \theta_2 = \pi/6)$, while (b) and (d) correspond to $(\theta_1 = \pi/6, \theta_2 = \pi/12)$. Cross-sections at $D = 0$ from [(a), (c)] and [(b), (d)] are depicted in (e) and (f), respectively, comparing the differences between the IPR (blue solid line) and IIPR (orange dashed line).

in equation (11), with the corresponding simulation results presented in figures 4(a) and (b). Within the arched region, several highly intense elongated zones, as well as a triangular area in the lower-left corner, are evident. Nevertheless, these high-intensity regions merely signify the existence of strongly confined localization and do not exclusively indicate the interfaced localization. In fact, strong localization in this system is not restricted to the atoms around the interface. A closer examination of figure 2 reveals that, in certain scenarios, the population becomes localized at one of the terminal atoms of the array, resulting in a single-edge excitation. For example, such behavior can be observed in the cross-section at $\xi \approx 0.6\pi$ in figure 2(b). To rigorously distinguish interfaced localization from single-edge excitation, we define the following measure called the interfaced IPR (IIPR):

$$\text{IIPR} \equiv \frac{\sum_{j' \in \text{interface}} \left(\Delta P_{j'}\right)^2}{\left(\sum_{j=1}^{N} \Delta P_j\right)^2}, \tag{12}$$

where the interface atoms are located at $j' \in \{m, m+1\}$ under the asymmetric driving scheme. If the IPR attains a maximum for certain parameters and coincides with the IIPR, this signifies interfaced localization. Conversely, if the two measures do not overlap and the IIPR reaches a minimum, it indicates the presence of single-edge excitation.

In figures 4(c) and (d), we present corresponding IIPR distributions of the parameters from figures 4(a) and (b), respectively. The results indicate that bright elongated regions in the IPR distribution disappear in the IIPR map, while the remaining bright areas primarily are concentrated in the triangular region at the lower left corner, which exactly corresponds to where interfaced localization occurs. This result further suggests that interfaced localization is most likely observed when the value of D is small, which aligned with the phenomenon we observed in figure 2. One can distinguish between these two types of excitation localization more clearly by comparing the cross-sections of the IPR and IIPR at $D = 0$, illustrated in figures 4(e) and (f), respectively. For instance, in figure 4(e), interfaced localization manifests in the range $\xi \in (0, 0.15\pi]$, while one-edge excitation emerges at $\xi = 0.25\pi$. Likewise, in figure 4(f), the interfaced localization can be revealed in two distinct intervals: $\xi \in (0, 0.2\pi]$ and $\xi \in [0.9\pi, \pi)$. In contrast, single-edge excitation appears around $\xi = 0.4\pi$. It should be noted that our analysis excludes scenarios involving extremely small interparticle separations, where near-field effects become significant [62, 63]. Thus, for an interatomic separation value of around $\xi \geqslant 0.1\pi$, these results could still remain valid. Overall, our defined IIPR and IPR calculations can faithfully identify the parameter regions

that can distinguish the interfaced localization from the single-edge excitation localization.

We note that as N increases, the trend of overlaps between IPR and IIPR near $\xi = 0$ and π is still sustained, indicating strong interfaced localizations. However, many more features emerge away from $\xi \approx 0$ or π, showing the intricate interplay between N and ξ. This can be explained and shown in equation (14) and figure 5 later in part C of section 3, where periodic or layered band structures depend on N and ξ. This can be attributed to the imparted traveling phases on the atoms and their interferences, which lead to unconverging IPR and IIPR when N increases, especially when ξ is away from 0 and π.

3.3. Size effect on interfaced localization

Here, we examine the excitation localizations under varying (θ_1, θ_2) with fixed (D, ξ). To further distinguish between interfaced localization and edge excitation, we introduce the ratio of interface-edge localization (RIEL), defined as

$$\mathrm{RIEL} = \frac{\tilde{P}_{\mathrm{interface}} - \tilde{P}_{\mathrm{edge}}}{\sum_{j=1}^{N} \tilde{P}_j}, \tag{13}$$

where $\tilde{P}_{\mathrm{interface}} = \tilde{P}_m + \tilde{P}_{m+1}$ and $\tilde{P}_{\mathrm{edge}} = \tilde{P}_1 + \tilde{P}_N$. As RIEL $\to 1$ (-1), the population distribution approaches and resembles interfaced localization (edge excitation). Here, we focus on the RIEL distribution under reciprocal coupling conditions ($D = 0$), where interfaced localization is most likely to manifest in low-D regimes, as shown in figure 5. Figures 5(a) and (b) reveal that RIEL exhibits a mirror-symmetric structure with respect to the diagonal $(\cos\theta_2 = -\cos\theta_1)$ in the $(\cos\theta_1, \cos\theta_2)$ space, forming banded structures. The triangle area in the lower right corner and other prominent bands suggest a higher propensity for interfaced localization when driven by the combination with a large θ_1 and a small θ_2. For instance, in figure 5(a), when $(\theta_1, \theta_2) = (0.9\pi, 0.1\pi)$, $\tilde{P}_{\mathrm{interface}} \approx 0.998$ is observed and similarly for $(\theta_1, \theta_2) = (0.75\pi, 0.25\pi)$, we find $\tilde{P}_{\mathrm{interface}} \approx 0.968$.

Moreover, these layered band structures exhibit angular periodicity associated with ξ. For a fixed system size N, five prominent bands appear within the lower triangular region of the heatmap when $\xi = 0.1\pi$ in figure 5(a). As ξ doubles, this region manifests ten bands in figure 5(b). With further increases in ξ, these bands gradually compress and merge, converging toward zero values, indicating delocalized distributions. Meanwhile, the lower-right triangle region retains its high intensity, despite steady reduction in size. Interfaced localization can only be sustained under asymmetrical driving of a larger θ_1 paired with a smaller θ_2. Such configurations effectively counteract the system's natural delocalization tendency induced by greater atomic separation.

Furthermore, by analyzing cross-sections along the diagonal (where $\cos\theta_2 = -\cos\theta_1$) of this distribution, we establish an empirical formula that captures the local minima

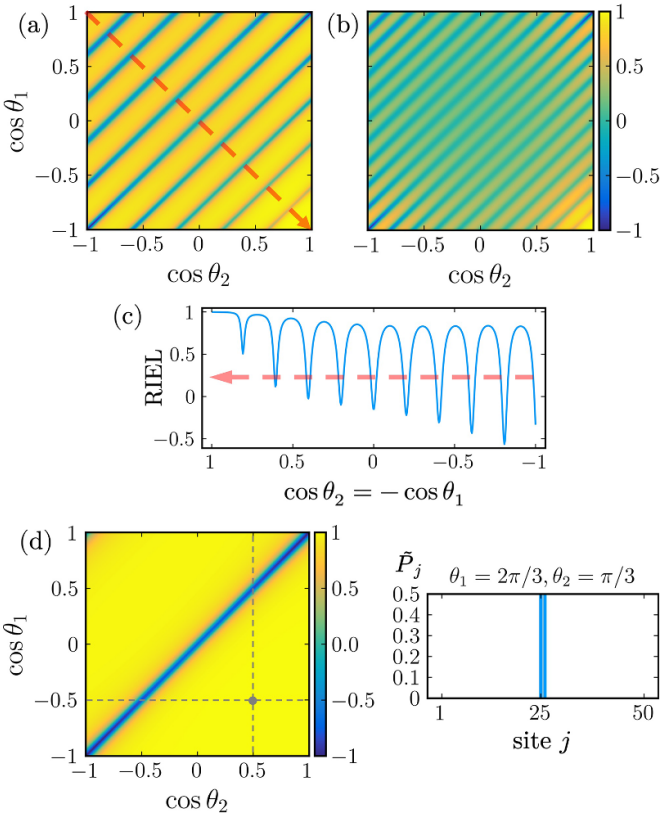

Figure 5. In the asymmetry-driving scheme, the RIEL is presented with respect to $(\cos\theta_1, \cos\theta_2)$. Panel (a) shows the RIEL distribution for $\xi = 0.1\pi$, while (b) corresponds to the case of $\xi = 0.2\pi$, both for $N = 100$. A cross-section along the diagonal of (a) is illustrated in (c), showcasing the distribution of RIEL's local minima. The left subplot in panel (d) shows the RIEL distribution for $N = 50$ and $\xi = 0.04\pi$. The right subplot displays the double-site atomic localization at the interface corresponding to the gray dot parameters $\theta_1 = 2\pi/3$ and $\theta_2 = \pi/3$ in the RIEL distribution.

of RIEL, which is

$$\cos\theta_1 - \cos\theta_2 = \frac{2n\pi}{m\xi}, \quad n \in \mathbb{Z}, \quad \xi \in (0, \pi), \tag{14}$$

where $n \in [1 - (m\xi/\pi), (m\xi/\pi) - 1]$, and $m = \lceil N/2 \rceil$ related to the system size N. For example, in figures 5(a) and (c), where $m\xi = 5\pi$, each local minimum along the diagonal is observed at $\cos\theta_2 = -\cos\theta_1 = n/5$, where $n \in [-4, 4]$. Therefore, equation (14) facilitates the prediction of RIEL distributions under $D = 0$ for different (N, ξ). Notably, as $m\xi \to \pi$, the RIEL displays a single trench of local minima along the anti-diagonal (where $\cos\theta_1 = \cos\theta_2$), with high-intensity regions predominating elsewhere. The results presented in figure 5(d) show excellent agreement with the prediction by equation (14). This indicates that the majority of angular combinations are inclined toward interfaced localization, apart from cases where $\theta_1 = \theta_2$. Conversely, when $m\xi \gg \pi$, concentrating atomic populations at the interface becomes progressively difficult, as more minimums emerge based on

equation (14). These patterns collectively underscore the substantial influence of system size on the formation of interfaced localization. As a side remark, we note that an optimal and significant interfaced localization emerges when the disparity between driving angles $(\theta_1 - \theta_2)$ increases. This can be seen in figures 5(a)–(c) when $\cos\theta_2 = -\cos\theta_1$ is near 1.

4. Defect-driving scheme

In the previously mentioned scheme, the phase distribution of the driving fields experienced by each atom is asymmetric. To explore more intriguing excitation localization in the steady states, we introduce the defect-driving scheme, where the driving field can be removed from one or multiple atoms, as illustrated in figure 1(b). In this scheme, it is assumed that the interatomic spacing is sufficiently large such that the fields Ω_1 and Ω_2 do not unintentionally excite the mth atom. The incident angles for the remaining atoms are defined as

$$\theta_j = \begin{cases} \theta_1 & ,j \in [1, m-1] \\ \pi - \theta_2 & ,j \in [m+1, N]\,. \end{cases} \tag{15}$$

The undriven mth atom distinguishes the array into a left- and a right chain, for which the phase reference point is set at the $(m-1)$th and the $(m+1)$th atom, respectively. This symmetry in phase distribution can be achieved by defining the Rabi frequencies with phases $\phi_1 = -k_0 x_{m-1}\cos\theta_1$ and $\phi_2 = -k_0 x_{m+1}\cos\theta_2$. Thus, the phase profile of the system attains symmetry with respect to the undriven atom. In this section, we focus on the defect-driving scheme under $D = 0$, as we believe and will demonstrate that, akin to asymmetrical driving schemes, this setup will yield pronounced interfaced localizations under reciprocal coupling.

4.1. Saturated population in interfaced localization

We first calculated the RIEL distribution for this driving scheme, where $\tilde{P}_{\text{interface}} = \tilde{P}_{m-1} + \tilde{P}_m + \tilde{P}_{m+1}$, with results shown in figures 6(a), (c) and (e). Notably, in most parameter regimes, RIEL remains non-negative, indicating the absence of strongly edged excitations. However, strong interfaced localizations are still observable. We can therefore identify the parameter ranges where strongly confined atomic localization occurs by examining only the population at the interface atoms.

Next, we analyze the distribution of $\tilde{P}_m$, the population at the undriven atom across various angular combinations (θ_1, θ_2) for specific values of ξ, as shown in figures 6(b), (d) and (f). For $\xi < 0.5\pi$, the maximum values of $\tilde{P}_m$ appear concentrated in a highlighted region in the upper right corner. As ξ approaches π, high-intensity regions emerge in all four corners of the heatmap, creating a perfectly symmetric distribution. Subsequently, we examine cross-sections along the anti-diagonal (where $\theta_1 = \theta_2 = \theta$) to compare the maximum values of $\tilde{P}_m$ across three distinct ξ values, as depicted in figure 7(a). These results suggest that a considerable population proportion on the undriven atom can most likely be observed under a small value of ξ, e.g. the profile for $\xi = 0.1\pi$ mostly surpasses those of the other cases significantly, reaching a peak of $\tilde{P}_m \approx 0.67$ at $\theta = 0.86\pi$. The corresponding driving configuration and resulting steady-state population distribution for this scenario are demonstrated in figure 7(b), revealing the strongest single-site excitation observed at the interface in this study so far, along with two accompanying tiny side lobes at the $(m-1)$th and the $(m+1)$th atoms. In fact, this localization demonstrates robustness against the non-guided decay up to $\gamma_{\text{ng}} \approx 0.5\gamma$.

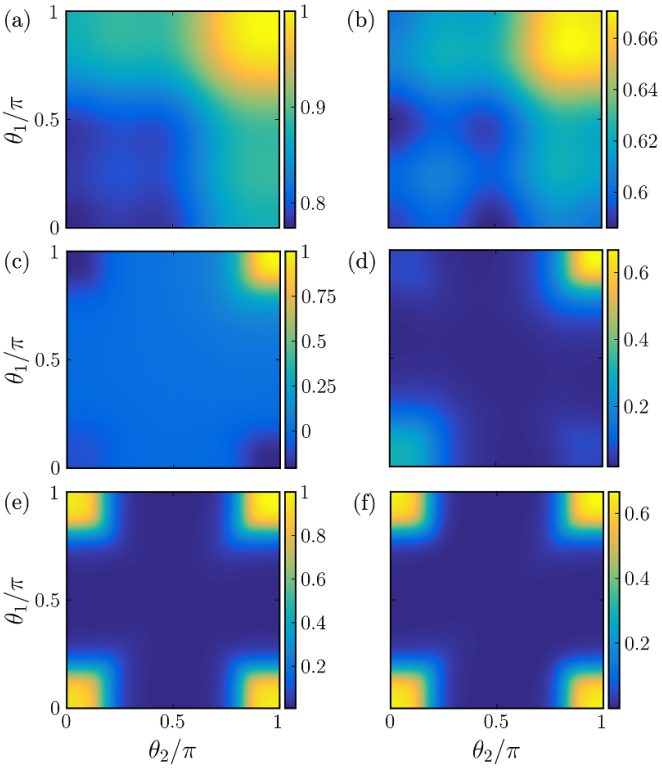

Figure 6. Within the defect-driven scheme, the distributions of the RIEL (panels (a), (c), and (e)) and the population of the non-driven atom $\tilde{P}_m$ (panels (b), (d), and (f)) are presented in the space (θ_1, θ_2). Panels [(a), (b)], [(c), (d)], and [(e), (f)] correspond to $\xi = 0.1\pi$, $\xi = 0.4\pi$, and $\xi = 0.95\pi$, respectively, showcasing the variation in distributions as the interatomic spacing increases. Other parameters are chosen at $N = 100$ and $D = 0$.

To further investigate the effect of ξ on $\tilde{P}_m$, we performed a scan over the range $\xi \in (0, \pi)$, with the findings displayed in figure 7(d). The regions, where the strong interfaced localization is most likely to occur, are primarily located along the right edge and bottom of the plot, covering a combined region of the entire θ range at low ξ values and the full ξ range at high θ values. Additionally, one can observe dark regions shaped like cave entrances where $\tilde{P}_m$ approaches 0, forming a hole excitation at the undriven atom. This dark region expands as the system size N increases, effectively compressing the parameter area for generating interfaced localization. To further

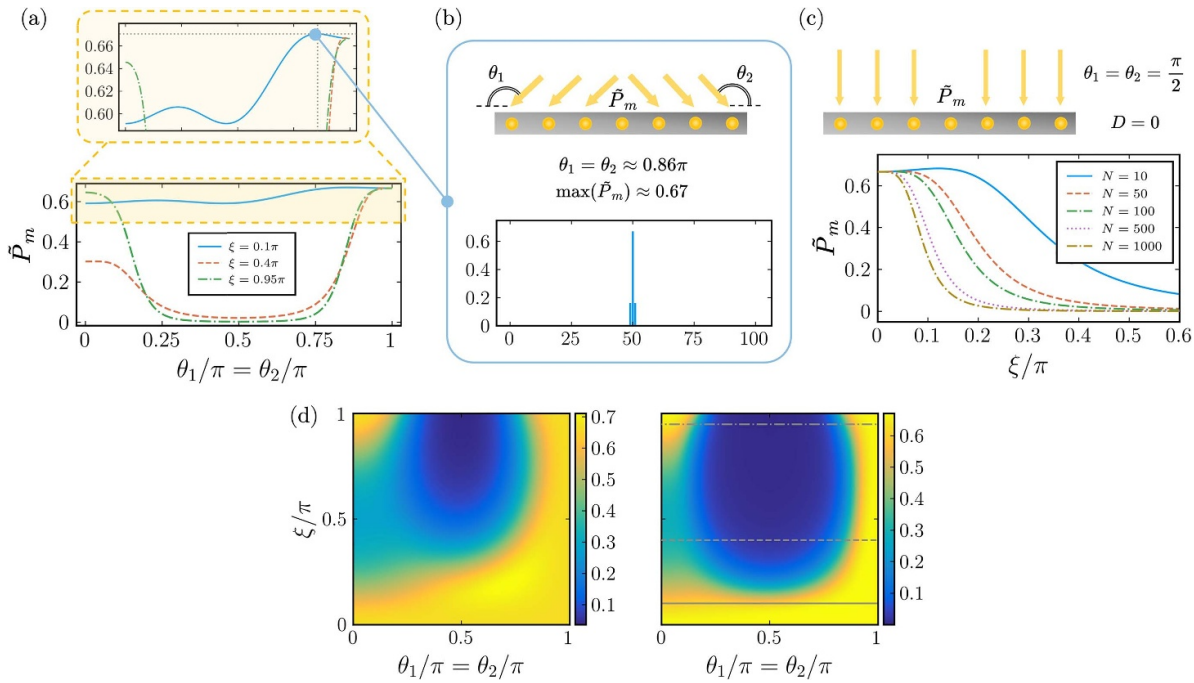

Figure 7. The saturation of the non-driven atom population $\tilde{P}_m$. (a) presents cross-sections along the anti-diagonal from figures 6(b), (d) and (f), depicting the variation of P_m with $\theta_1 = \theta_2 = \theta$ for $D = 0$ and specific interatomic distances: $\xi = 0.1\pi$ (blue solid line), $\xi = 0.4\pi$ (orange dashed line), and $\xi = 0.95\pi$ (green dotted line). (b) showcases the corresponding maximum of the blue solid line ($D = 0$, $\xi = 0.1\pi$) from (a), showing that under antisymmetric driving at $\theta_1 = \theta_2 \approx 0.86\pi$, $\tilde{P}_m$ reaches a maximum value of approximately 0.67. (c) demonstrates how $\tilde{P}_m$ varies with interparticle distance ξ under normal incidence for different atom numbers $N = 10$ (blue solid line), $N = 50$ (orange dashed line), $N = 100$ (green dash–dot line), $N = 500$ (purple dotted line), and $N = 1000$ (brown dash–dot line). The results reveal that as $\xi \to 0$ (i.e. 2π), $\tilde{P}_m$ saturates to exactly $2/3$, regardless of N. (d) compares the $\tilde{P}_m$ distribution for $N = 10$ and $N = 100$ in the left and right subplots, respectively, where the gray solid-, dashed-, and dash–dotted line correspond to the curves with the same styles in (a).

corroborate this phenomena, we examine the vertical cross-section of these colormaps under $\theta_1 = \theta_2 = \pi/2$ for various system sizes, with N ranging from 10 to 1000, as shown in figure 7(c). It is clear that as the system size grows, the maximally attainable $\tilde{P}_m$ converges to a numerical value of approximately 0.667, which we refer to as the 'saturated population'. Concurrently, the interparticle distance ξ, where saturation occurs, approaches 0 (or 2π). Such behaviors can be explained through the analytical solution presented below in equation (16).

4.2. Analytical solutions

Here, we present the analytical solutions for the configuration depicted in figure 7(c), where $\theta_1 = \theta_2 = \pi/2$ and $D = 0$. The steady-state probability amplitudes $\{\tilde{p}_j\}$ can be derived analytically through equation (8) and are given by

$$\tilde{p}_j = -\Omega \begin{cases} \mathrm{i} + \tan(\xi/2) & , j = 1, N \\ 2\csc\xi & , j = m \\ -2\cot\xi + \csc\xi & , j = m-1, m+1 \\ 2\tan(\xi/2) & , \text{other} \end{cases}, \tag{16}$$

where $N \geqslant 5$. From this, one can derive the population $\tilde{P}_m$ of the undriven atom, yielding the expression

$$\frac{2\csc^2\xi}{1 - 4\cot\xi\tan\left(\frac{\xi}{2}\right) + 3\csc^2\xi + (2N-9)\tan^2\left(\frac{\xi}{2}\right)}. \tag{17}$$

In the limiting case, we obtain a saturation value $\lim_{\xi\to 0\,(2\pi)} \tilde{P}_m = 2/3$ regardless of N, which aligns excellently with the numerical output. Similarly, we have $\lim_{\xi\to 0\,(2\pi)} \tilde{P}_{m\pm1} = 1/6$. In fact, these results hold true for any $\theta \in (0, \pi)$, revealing the robustness of saturated population against varying incident angles. In other words, the population distribution becomes fully concentrated at the interface atoms, predominantly at the undriven atom as $\xi \to 0$ (or 2π), leading to pronounced single-site localization. In addition, we provide the interatomic distances, denoted as $\xi_{\max}$, at which $\tilde{P}_m$ reaches its maximum for various system sizes N. The result can be expressed as

$$\xi_{\max} = 2k\pi + 2\tan^{-1}\left(\frac{1}{\sqrt{4N-13}}\right), \tag{18}$$

where $k \in \mathbb{Z}$. This $\xi_{\max}$ clearly approaches 0 (or $2k\pi$) as N increases, a trend that perfectly matches the observations in figure 7(c).

In summary, as N increases, the maximum achievable population at the undriven atom gradually decreases and converges to the saturation value of $2/3$. Correspondingly, the optimal interatomic distance also approaches $2k\pi$. This phenomenon can be attributed to the competition between the number of atoms and the spin-exchange interactions. As the system size expands, the driven atoms with increasing number carve the population of the undriven atom up and redistributes it into other atomic sites, diminishing the interfaced localization. However, under the influence of strong RDDI (when $\xi \to 0$ or 2π), the population of the undriven atom remains saturated. In contrast, in smaller systems, the population at the interface atoms can slightly exceed the saturation threshold. For example, with $N = 5$, we observe $\max(\tilde{P}_m) \approx 0.723 > 2/3$, with corresponding $\tilde{P}_{1,N} \approx 0.092$, and $\tilde{P}_{\text{others}} \approx 0.044$. This observation reflects the subtle competition between system size and RDDI strength within chirally coupled atomic-waveguide systems.

To elaborate more on the mechanism toward the saturation values, we resort to the Dicke Hamiltonian [64] for more insights. The condition of $\xi = 2\pi$ reduces our system to the Dicke Hamiltonian, where uncoupled superradiant and subradiant sectors can be formed. These driven atoms would show superradiant emissions as predicted in the Dicke Hamiltonian under an initially inverted system condition. Meanwhile, the driven atoms at the interfaces manifest a less saturated value of $1/6$, which again shows the essence of the interfaces and superradiance effect that dissipates the atoms more quickly. We note that for the Dicke Hamiltonian with $\xi = 2\pi$ under driving conditions, the driving fields unavoidably populate all the atoms in the symmetric superradiant sectors, where our weak-field excitation approximation breaks down. This also shows in equation (16), where a divergence of probability amplitude emerges. Therefore, the slight accumulation at the interfaces in figures 7 and 8 can be explained by the system moving slightly away from the Dicke Hamiltonian at $\xi \neq 2\pi$, opening the spin-exchange channels between the superradiant and subradiant sectors not allowed in the Dicke Hamiltonian. We conjecture that the undriven atoms would be populated via spin-exchange interactions and become saturated even under spontaneous decays. The outcome of this saturated value can be balanced from a competition between population transfer from driven atoms and its own decay. The saturated value of $2/3$ for the undriven atom thus can be attributed to some subradiant state sectors that have little decays, and its strong localization is manifested due to the intricate interference among these states.

4.3. Precise localization control

By selectively excluding the excitation of a single atom, we induce a robust single-site localization, with the flexibility to reposition this localized excitation by designating different undriven atoms, which offers a framework for precise localization control. This leads to a natural question: what if multiple atoms are left undriven under the same angular configuration? The results, depicted in figure 8, explore this scenario. Specifically, in figure 8(a), we analyze a 1D array of 20 atoms, driven under the same parameters in figure 7(b). Intriguingly, when the excitation field is removed from two adjacent atoms (the 10th and 11th atoms in this instance), the population distributes evenly across these two undriven atoms and their neighboring driven atoms, as illustrated by the red bars in figure 8(a). This configuration effectively truncates population, isolating it to these four atoms. Upon extending the removal to three or even four neighboring atoms, we observe a progressive separation of the distribution, with localization occurring solely at the endpoints of the undriven cluster and their adjacent driven atoms, establishing a controllable approach to excitation localization. Finally, in figure 8(b), we demonstrate an alternative approach for structuring localization distributions. By removing the excitation from non-adjacent atoms in a 1D array, the precise multiple-site localization can be achieved, potentially offering a practical route toward quantum memory implementation.

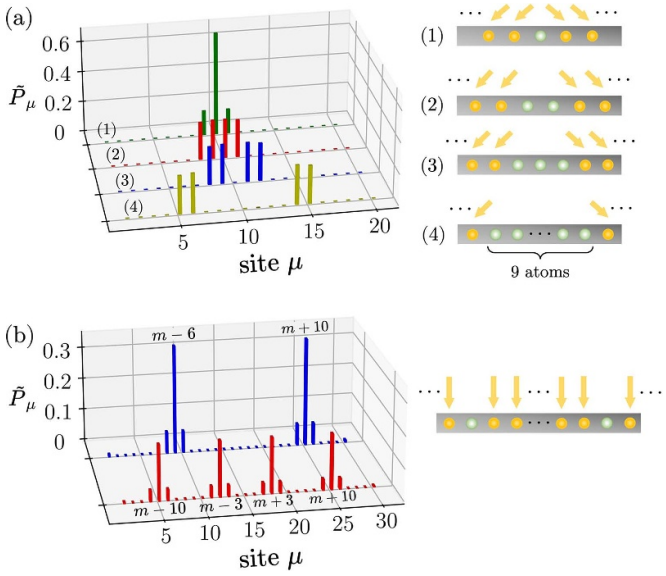

Figure 8. Precise control of localization under the defect-driven scheme. (a) shows the case of $N = 20$ atoms under the same parameters in figure 7(b), where removing the driving field from (1) a single atom, (2) two atoms, (3) three atoms, and (4) nine atoms inside (with non-driven atoms shown in green) results in accumulated populations at the two atoms at the ends of the non-driven array and their neighboring sites. (b) demonstrates a method of removing the driving field from several non-adjacent atoms. For $N = 30$ atoms, two-site localization depicted in the blue bars is achieved by removing the driving from $(m-6)$th and $(m+10)$th atoms, while the red bars illustrate four-site localization resulting from excluding the driving from four non-adjacent atoms $(m-10, m-3, m+3,$ and $m+10)$, with $m = 15$.

For experimental feasibility, we can implement these atomic arrays coupled to PCWs [1, 3, 28] under the strong coupling regime. To scale up these atomic arrays, optical lattices can be applied to trap and manipulate them [19], while

to better control the atoms' positions, optical tweezers [30] can be utilized. Our driving schemes can be set up from side excitations on individual constituents [10] without crosstalks since atoms can still be effectively coupled at long distances due to the nature of long-range dipole–dipole interactions [20]. However, one main limitation lies at the demanding coupling efficiency to genuinely showcase the strong localization of atomic excitations. In this perspective, quantum dots or superconducting qubits are better candidates to achieve an even higher coupling regime [1].

5. Conclusion

In conclusion, a 1D open system of atomic arrays coupled to a waveguide under weak driving forms a distinctive driven-dissipative quantum system capable of exhibiting rich non-equilibrium dynamics and steady-state phases. This arises from the intricate interplay among the competition between long-range dipole–dipole interactions and coupling directionality. By adjusting the incident angles of laser fields, traveling phase differences are introduced, effectively modulating the system's behaviors. We divided the homogeneous array into two subchains, each driven asymmetrically at different angles. This approach, combined with tailored Rabi frequency phase settings, produced strongly localized population distributions. Notably, under the reciprocal coupling regime, adjusting the system size N and atomic separation ξ to satisfy $N\xi \to 2\pi$ enables strongly localized two-site interfaced atomic states with maximal observation probability across various angle combinations. Additionally, precise control over the spatial positioning of this two-site localization can be realized by only shifting the position of the interface between the two subchains, which creates a mechanism to excite population to specific atomic sites. We further redesigned this scheme by removing the laser field on one interfaced atom, designating it as the boundary between the two subchains as a defect-driving scheme. By adjusting the phase of the Rabi frequency, we achieved a more symmetric effective traveling phase. Under these conditions and at a interparticle spacing close to a period of 2π, the saturated population can be observed at the undriven atom, yielding the strongest single-site localization in this study with notable robustness against non-guided decay. This outcome is well-supported by analytical solutions under reciprocal coupling conditions. Our results sheds light on driven-dissipative quantum systems with nonreciprocal coupling, paving the way for quantum simulations of exotic many-body states—a development with significant implications for quantum information applications.

Data availability statement

All data that support the findings of this study are included within the article (and any supplementary files).

Acknowledgments

We acknowledge support from the National Science and Technology Council (NSTC), Taiwan, under the Grant Nos. NSTC-112-2119-M-001-007 and NSTC-112-2112-M-001-079-MY3, and from Academia Sinica under Grant AS-CDA-113-M04. We are also grateful for support from TG 1.2 of NCTS at NTU.

ORCID iDs

Shao-Hung Chung https://orcid.org/0009-0001-6148-4200
Wei Chen https://orcid.org/0009-0005-4884-352X
H H Jen https://orcid.org/0000-0002-1152-8164

References

[1] Sheremet A S, Petrov M I, Iorsh I V, Poshakinskiy A V and Poddubny A N 2023 Waveguide quantum electrodynamics: collective radiance and photon-photon correlations *Rev. Mod. Phys.* **95** 015002
[2] Lodahl P, Mahmoodian S, Stobbe S, Rauschenbeutel A, Schneeweiss P, Volz J, Pichler H and Zoller P 2017 Chiral quantum optics *Nature* **541** 473
[3] Chang D E, Douglas J S, González-Tudela A, Hung C-L and Kimble H J 2018 Colloquium: quantum matter built from nanoscopic lattices of atoms and photons *Rev. Mod. Phys.* **90** 031002
[4] Masson S J and Asenjo-Garcia A 2020 Atomic-waveguide quantum electrodynamics *Phys. Rev. Res.* **2** 043213
[5] Kim E, Zhang X, Ferreira V S, Banker J, Iverson J K, Sipahigil A, Bello M, González-Tudela A, Mirhosseini M and Painter O 2021 Quantum electrodynamics in a topological waveguide *Phys. Rev. X* **11** 011015
[6] Fayard N, Henriet L, Asenjo-Garcia A and Chang D E 2021 Many-body localization in waveguide quantum electrodynamics *Phys. Rev. Res.* **3** 033233
[7] Suárez-Forero D G, Mehrabad M J, Vega C, González-Tudela A and Hafezi M 2024 Chiral quantum optics: recent developments and future directions (arXiv:2411.06495 [physics.optics])
[8] Jen H H 2024 Photon-mediated dipole-dipole interactions as a resource for quantum science and technology in cold atoms (arXiv:2410.20665 [quant-ph])
[9] Bliokh K Y and Nori F 2015 Transverse and longitudinal angular momenta of light *Phys. Rep.* **592** 1
[10] Mitsch R, Sayrin C, Albrecht B, Schneeweiss P and Rauschenbeutel A 2014 Quantum state-controlled directional spontaneous emission of photons into a nanophotonic waveguide *Nat. Commun.* **5** 5713
[11] Ramos T, Pichler H, Daley A J and Zoller P 2014 Quantum spin dimers from chiral dissipation in cold-atom chains *Phys. Rev. Lett.* **113** 237203
[12] Pichler H, Ramos T, Daley A J and Zoller P 2015 Quantum optics of chiral spin networks *Phys. Rev. A* **91** 042116
[13] Luxmoore I J, Wasley N A, Ramsay A J, Thijssen A C T, Oulton R, Hugues M, Kasture S, Achanta V G, Fox A M and Skolnick M S 2013 Interfacing spins in an InGaAs quantum dot to a semiconductor waveguide circuit using emitted photons *Phys. Rev. Lett.* **110** 037402

[14] Arcari M *et al* 2014 Near-unity coupling efficiency of a quantum emitter to a photonic crystal waveguide *Phys. Rev. Lett.* **113** 093603
[15] Yalla R, Sadgrove M, Nayak K P and Hakuta K 2014 Cavity quantum electrodynamics on a nanofiber using a composite photonic crystal cavity *Phys. Rev. Lett.* **113** 143601
[16] Söllner I *et al* 2015 Deterministic photon–emitter coupling in chiral photonic circuits *Nat. Nanotechnol.* **10** 775
[17] Roushan P *et al* 2017 Chiral ground-state currents of interacting photons in a synthetic magnetic field *Nat. Phys.* **13** 146
[18] Wang D-W *et al* 2019 Synthesis of antisymmetric spin exchange interaction and chiral spin clusters in superconducting circuits *Nat. Phys.* **15** 382
[19] Corzo N V, Raskop J, Chandra A, Sheremet A S, Gouraud B and Laurat J 2019 Waveguide-coupled single collective excitation of atomic arrays *Nature* **566** 359
[20] Solano P, Barberis-Blostein P, Fatemi F K, Orozco L A and Rolston S L 2017 Super-radiance reveals infinite-range dipole interactions through a nanofiber *Nat. Commun.* **8** 1857
[21] Sayrin C, Clausen C, Albrecht B, Schneeweiss P and Rauschenbeutel A 2015 Storage of fiber-guided light in a nanofiber-trapped ensemble of cold atoms *Optica* **2** 353
[22] Dong Y, Taylor J, Lee Y S, Kong H R and Choi K S 2021 Waveguide-qed platform for synthetic quantum matter *Phys. Rev. A* **104** 053703
[23] Sipahigil A *et al* 2016 An integrated diamond nanophotonics platform for quantum-optical networks *Science* **354** 847
[24] Bhaskar M K *et al* 2017 Quantum nonlinear optics with a germanium-vacancy color center in a nanoscale diamond waveguide *Phys. Rev. Lett.* **118** 223603
[25] Vetsch E, Reitz D, Sagué G, Schmidt R, Dawkins S T and Rauschenbeutel A 2010 Optical interface created by laser-cooled atoms trapped in the evanescent field surrounding an optical nanofiber *Phys. Rev. Lett.* **104** 203603
[26] Kim M E, Chang T-H, Fields B M, Chen C-A and Hung C-L 2019 Trapping single atoms on a nanophotonic circuit with configurable tweezer lattices *Nat. Commun.* **10** 1647
[27] Thompson J D, Tiecke T G, de Leon N P, Feist J, Akimov A V, Gullans M, Zibrov A S, Vuletić V and Lukin M D 2013 Coupling a single trapped atom to a nanoscale optical cavity *Science* **340** 1202
[28] Goban A, Hung C-L, Hood J D, Yu S-P, Muniz J A, Painter O and Kimble H J 2015 Superradiance for atoms trapped along a photonic crystal waveguide *Phys. Rev. Lett.* **115** 063601
[29] Jen H H 2020 Disorder-assisted excitation localization in chirally coupled quantum emitters *Phys. Rev. A* **102** 043525
[30] Dordevic T, Samutpraphoot P, Ocola P L, Bernien H, Grinkemeyer B, Dimitrova I, Vuletić V and Lukin M D 2021 Entanglement transport and a nanophotonic interface for atoms in optical tweezers *Science* **373** 1511
[31] Iversen O A and Pohl T 2022 Self-ordering of individual photons in waveguide qed and rydberg-atom arrays *Phys. Rev. Res.* **4** 023002
[32] Fedorovich G, Kornovan D, Poddubny A and Petrov M 2022 Chirality-driven delocalization in disordered waveguide-coupled quantum arrays *Phys. Rev. A* **106** 043723
[33] Henriet L, Douglas J S, Chang D E and Albrecht A 2019 Critical open-system dynamics in a one-dimensional optical-lattice clock *Phys. Rev. A* **99** 023802
[34] Zhang Y-X and K Mølmer 2019 Theory of subradiant states of a one-dimensional two-level atom chain *Phys. Rev. Lett.* **122** 203605
[35] Ke Y, Poshakinskiy A V, Lee C, Kivshar Y S and Poddubny A N 2019 Inelastic scattering of photon pairs in qubit arrays with subradiant states *Phys. Rev. Lett.* **123** 253601
[36] Albrecht A, Henriet L, Asenjo-Garcia A, Dieterle P B, Painter O and Chang D E 2019 Subradiant states of quantum bits coupled to a one-dimensional waveguide *New J. Phys.* **21** 025003
[37] Jen H H, Chang M-S, Lin G-D and Chen Y-C 2020 Subradiance dynamics in a singly excited chirally coupled atomic chain *Phys. Rev. A* **101** 023830
[38] Mahmoodian S, Calajó G, Chang D E, Hammerer K and Srensen A S 2020 Dynamics of many-body photon bound states in chiral waveguide qed *Phys. Rev. X* **10** 031011
[39] Jen H H 2021 Bound and subradiant multiatom excitations in an atomic array with nonreciprocal couplings *Phys. Rev. A* **103** 063711
[40] Pennetta R, Blaha M, Johnson A, Lechner D, Schneeweiss P, Volz J and Rauschenbeutel A 2022 Collective radiative dynamics of an ensemble of cold atoms coupled to an optical waveguide *Phys. Rev. Lett.* **128** 073601
[41] Pennetta R, Lechner D, Blaha M, Rauschenbeutel A, Schneeweiss P and Volz J 2022 Observation of coherent coupling between super- and subradiant states of an ensemble of cold atoms collectively coupled to a single propagating optical mode *Phys. Rev. Lett.* **128** 203601
[42] Needham J A, Lesanovsky I and Olmos B 2019 Subradiance-protected excitation transport *New J. Phys.* **21** 073061
[43] Wu C-C, Lin K-T, Handayana I G N Y, Chien C-H, Goswami S, Lin G-D, Chen Y-C and Jen H H 2024 Atomic excitation delocalization at the clean to disordered interface in a chirally-coupled atomic array *Phys. Rev. Res.* **6** 013159
[44] Chung S-H, Handayana I G N Y, Tsao Y-L, Wu C-C, Lin G-D and Jen H H 2024 Steady-state phases and interaction-induced depletion in a driven-dissipative chirally-coupled dissimilar atomic array *Phys. Rev. Res.* **6** 023232
[45] Handayana I G N Y, Wu C-C, Goswami S, Chen Y-C and Jen H H 2024 Atomic excitation trapping in dissimilar chirally coupled atomic arrays *Phys. Rev. Res.* **6** 013320
[46] Léonard J, Kim S, Rispoli M, Lukin A, Schittko R, Kwan J, Demler E, Sels D and Greiner M 2023 Probing the onset of quantum avalanches in a many-body localized system *Nat. Phys.* **19** 481
[47] González-Tudela A and Porras D 2013 Mesoscopic entanglement induced by spontaneous emission in solid-state quantum optics *Phys. Rev. Lett.* **110** 080502
[48] Mahmoodian S, Čepulkovskis M, Das S, Lodahl P, Hammerer K and A S Sørensen 2018 Strongly correlated photon transport in waveguide quantum electrodynamics with weakly coupled emitters *Phys. Rev. Lett.* **121** 143601
[49] Downing C A, Carre no J C L, Fernández-Domínguez A I and del Valle E 2020 Asymmetric coupling between two quantum emitters *Phys. Rev. A* **102** 013723
[50] Le Jeannic H *et al* 2021 Experimental reconstruction of the few-photon nonlinear scattering matrix from a single quantum dot in a nanophotonic waveguide *Phys. Rev. Lett.* **126** 023603
[51] Jen H H 2022 Quantum correlations of localized atomic excitations in a disordered atomic chain *Phys. Rev. A* **105** 023717
[52] Luo Y-K, Yang Y, Lu J and Zhou L 2023 Control of a single-photon router via an extra cavity *Appl. Phys. Lett.* **123** 211103
[53] Olmos B, Liedl C, Lesanovsky I and Schneeweiss P 2021 Bragg condition for scattering into a guided optical mode *Phys. Rev. A* **104** 043517
[54] Poddubny A N 2022 Driven anti-Bragg subradiant correlations in waveguide quantum electrodynamics *Phys. Rev. A* **106** L031702

[55] Kirova T, Jia N, Asadpour S H, Qian J, Juzeliūnas G and Hamedi H R 2020 Strongly confined atomic localization by Rydberg coherent population trapping *Opt. Lett.* **45** 5440
[56] Cardenas-Lopez S, Masson S J, Zager Z and Asenjo-Garcia A 2023 Many-body superradiance and dynamical mirror symmetry breaking in waveguide QED *Phys. Rev. Lett.* **131** 033605
[57] Lehmberg R H 1970 Radiation from an *n*-atom system. I. general formalism *Phys. Rev. A* **2** 883
[58] Le Kien F and Rauschenbeutel A 2017 Nanofiber-mediated chiral radiative coupling between two atoms *Phys. Rev. A* **95** 023838
[59] Jen H H 2020 Steady-state phase diagram of a weakly driven chiral-coupled atomic chain *Phys. Rev. Res.* **2** 013097
[60] Murphy N C, Wortis R and Atkinson W A 2011 Generalized inverse participation ratio as a possible measure of localization for interacting systems *Phys. Rev. B* **83** 184206
[61] Lidar D A, Chuang I L and Whaley K B 1998 Decoherence-free subspaces for quantum computation *Phys. Rev. Lett.* **81** 2594
[62] Fiscelli G, Rizzuto L and Passante R 2018 Resonance energy transfer between two atoms in a conducting cylindrical waveguide *Phys. Rev. A* **98** 013849
[63] Kuraptsev A S and Sokolov I M 2020 Incomplete spontaneous decay in a waveguide caused by polarization selection *Phys. Rev. A* **101** 053852
[64] Dicke R H 1954 Coherence in spontaneous radiation processes *Phys. Rev.* **93** 99